Numerical simulation of turbulent flow in an axisymmetric diffuser with a curved surface centre-body

Received May 1996
Revised May 1997
Accepted August 1997

D. Xu and B.C. Khoo
Mechanical and Production Engineering Department, National University of Singapore, Singapore, and
M.A. Leschziner
Mechanical Engineering Department, UMIST, Manchester, UK

1. Introduction

Flow separation and reattachment are very common features in most flows of engineering interest, and phenomena associated with separation very often dominate the flow fields in that they can drastically alter the efficiency of the said engineering devices. A classical example is found in external flows. There is a dramatic increase in form drag associated with flow separation over a streamlined or bluff body with graver consequence for the former since form drag without flow separation only constitutes a relatively much smaller component of overall drag. However, many engineering devices operate at their highest efficiency with the flow close to separation. It is this occurrence which has led to intensive research in this area.

The principal objective of the present research effort is to employ and compare the various commonly used general turbulence models that can still predict the effects of flow curvature on the turbulence structure of the associated boundary layer. One important outcome of the present work is the ability to predict the separation and reattachment of turbulent flows inside an axisymmetric diffuser with a curved surface centre-body. Such findings can be naturally extended to a wide range of flows such as those over wings of aeroplanes and cascades of airfoils where flow separation and attachment occur over surfaces with geometrical curvature.

2. Mathematical formulations

2.1 Governing equation

In tensor notation, the incompressible, two-dimensional, steady state, time-averaged Navier-Stokes equations of motion and continuity of fluid are given below

$$U_j \frac{\partial U_i}{\partial x_j} = -\frac{\partial}{\rho \partial x_i}\left(P + \frac{2}{3}\rho k\right) + \frac{\partial}{\partial x_j}\left[(\nu + \nu_t)\left(\frac{\partial U_i}{\partial x_j} + \frac{\partial U_j}{\partial x_i}\right)\right] \quad (1)$$

International Journal of Numerical Methods for Heat & Fluid Flow
Vol. 8 No. 2, 1998, pp. 245–255.

$$\frac{\partial U_i}{\partial x_i} = 0 \tag{2}$$

where the symbols used take on their usual meanings.

2.2 Turbulence models

Equations (1) and (2) by themselves are not closed because of the turbulent kinetic energy term (k) and turbulent viscosity term (ν_t). To enable the closure of the time-averaged Navier-Stokes equations, one has to find effective and suitable equations relating k and ν_t. Shown below are the various models employed in the present work.

2.2.1 One-equation turbulence model (Wolfshtein model). In the standard one-equation model, the kinetic energy k can be obtained from the standard modelled transport equation:

$$U_i \frac{\partial k}{\partial x_i} = \nu_t \frac{\partial U_i}{\partial x_j}\left(\frac{\partial U_i}{\partial x_j} + \frac{\partial U_j}{\partial x_i}\right) + \frac{\partial}{\partial x_i}\left[\left(\nu + \frac{\nu_t}{\sigma_k}\right)\frac{\partial k}{\partial x_i}\right] - \varepsilon \tag{3}$$

Here ν_t is obtained from the Wolfshtein model (Wolfshtein, 1969):

$$\nu_t = C_\mu k^{1/2} l_\mu \tag{4}$$

$$\varepsilon = C_D k^{3/2} / l_D \tag{5}$$

2.2.2 Two-equation k-ε *turbulence models.* There are four different two-equation k-ε turbulence models used in the present study. All these models are briefly listed below. The interested reader should refer to the respective references given for details.

2.2.2.1 High-Reynolds number k-ε *turbulence model.* In the region away from the wall (i.e. $y^+ > 60$), the standard high-Reynolds number version of the k-ε model, originally devised by Launder and Spalding (1972), was adopted. The turbulent kinetic energy is still governed by equation (3), as in the one-equation model, except that the rate of dissipation (ε) in that equation is now obtained from a modelled transport equation:

$$U_i \frac{\partial \varepsilon}{\partial x_i} = \frac{\partial}{\partial x_i}\left[\left(\nu + \frac{\nu_t}{\sigma_\nu}\right)\frac{\partial \varepsilon}{\partial x_i}\right] + C_{\varepsilon 1}\frac{\varepsilon}{k}\nu_t\left(\frac{\partial U_i}{\partial x_j} + \frac{\partial U_j}{\partial x_i}\right)\frac{\partial U_i}{\partial x_j} - C_{\varepsilon 2}\frac{\varepsilon^2}{k} \tag{6}$$

with

$$\nu_t = C_\mu \frac{k^2}{\varepsilon} \tag{7}$$

The purpose for the form of the ε equation used is that it has been tested extensively in computations of shear-free flows and wall flows, and has proven to be rather successful (Launder and Spalding, 1972; 1974; Launder *et al.*, 1972).

This high-Reynolds number turbulence model, however, cannot be applied to the near wall region where the viscosity is dominant. In this work, either the one equation turbulence model (i.e. Wolfshtein's model) or the wall function method is used to determine the flow variables in the near wall region.

2.2.2.2 Low-Reynolds number k-ε *turbulence model.* In the near wall region, a more general low-Reynolds number turbulent model is required, in which the turbulent viscosity can be determined purely through the transport equations. In the present study, Launder-Sharma's low-Reynolds number *k-ε* model (Launder and Sharma, 1974) is adopted, which is given as

$$U_i\frac{\partial k}{\partial x_i}=\nu_t\frac{\partial U_i}{\partial x_j}\left(\frac{\partial U_i}{\partial x_j}+\frac{\partial U_j}{\partial x_i}\right)+\frac{\partial}{\partial x_i}\left[\left(\nu+\frac{\nu_t}{\sigma_k}\right)\frac{\partial k}{\partial x_i}\right]-\bar{\varepsilon}-2\nu\left(\frac{\partial\sqrt{k}}{\partial x_j}\right)^2 \tag{8}$$

$$U_i\frac{\partial\bar{\varepsilon}}{\partial x_i}=\frac{\partial}{\partial x_i}\left[\left(\nu+\frac{\nu_t}{\sigma_\nu}\right)\frac{\partial\bar{\varepsilon}}{\partial x_i}\right]+C_{\varepsilon 1}\frac{\bar{\varepsilon}}{k}\nu_t\left(\frac{\partial U_i}{\partial x_j}+\frac{\partial U_j}{\partial x_i}\right)\frac{\partial U_i}{\partial x_j}-C'_{\varepsilon 2}\frac{\bar{\varepsilon}^2}{k}+2\nu\nu_t\left(\frac{\partial^2 U_i}{\partial x_j\partial x_k}\right)^2 \tag{9}$$

where

$$\bar{\varepsilon}=\varepsilon-2\nu\left(\partial\sqrt{k}/\partial x_j\right)^2 \tag{10}$$

2.2.2.3 RNG k-ε *turbulence model.* Like the high Reynolds number *k-ε* turbulence model, the RNG (renormalization group) *k-ε* model uses the same turbulent kinetic energy equation (equation (3)), and employs an additional source/sink term in the *ε* equation with various model coefficients. The form of the *ε* equation of the RNG *k-ε* model is as follows (Yakhot *et al.*, 1992):

$$U_i\frac{\partial\varepsilon}{\partial x_i}=\frac{\partial}{\partial x_i}\left[\left(\nu+\frac{\nu_t}{\sigma_\nu}\right)\frac{\partial\varepsilon}{\partial x_i}\right]+C_{\varepsilon 1}\frac{\varepsilon}{k}\nu_t\left(\frac{\partial U_i}{\partial x_j}+\frac{\partial U_j}{\partial x_i}\right)\frac{\partial U_i}{\partial x_j}-\frac{c_\mu\eta^3(1-\eta/\eta_0)}{1+\beta\eta^3}\frac{\varepsilon^2}{k}-C_{\varepsilon 2}\frac{\varepsilon^2}{k} \tag{11}$$

2.2.2.4 Anisotropic model. The form of this model is fairly identical to that of the high Reynolds number turbulence model. The difference lies in the value of constants $C_{\varepsilon 1}$ and $C_{\varepsilon 2}$ which are obtained as follows:

$$C_{\varepsilon 1}=1.125 \tag{12}$$

$$C_{\varepsilon 2}=\frac{1.92}{(1+0.9A^{1/2}A_2)} \tag{13}$$

In the present study, the eddy-viscosity model according to Launder and Suga (1993) is employed.

3. Numerical solution

3.1 Discretisation of governing equations

The governing equations may be summarised as follows

$$\frac{\partial}{\partial x_j}(U_j\phi)=\frac{\partial}{\partial x_j}\left(\Gamma_\phi\frac{\partial\phi}{\partial x_j}\right)+S_\phi \tag{14}$$

where ϕ is a general dependent variable which may stand for U_i, k and ε; Γ_ϕ is the diffusive coefficient, and S_ϕ represents all the source terms which cannot be expressed as either convection or diffusion. Using control volume methods, equation (14) is integrated over a control volume surrounding P, as shown in Figure 1,

$$\int\int_V \left[\frac{\partial}{\partial x}(U\phi) - \frac{\partial}{\partial x}\left(\Gamma_\phi \frac{\partial \phi}{\partial x}\right) + \frac{\partial}{\partial y}(V\phi) - \frac{\partial}{\partial y}\left(\Gamma_\phi \frac{\partial \phi}{\partial y}\right)\right] dV = \int\int_V S_\phi \, dV \quad (15)$$

Applying Gauss' theorem, the volume integral on the left-hand side may be expressed in terms of surface integral; equation (15) can thus be rewritten as:

$$F_e - F_w + F_n - F_s = \overline{S_\phi} \bullet Vol \quad (16)$$

where the subscripts e, w, n and s indicate the east, west, north and south faces of the control volume, respectively. With the approximations for convection, diffusion and the source terms, Equation (16) may be rearranged in a way such as:

$$(A_P - S_P)\phi_P = \sum A_n \phi_n + S_U \quad (17)$$

Equation (17) is then solved by a "line-by-line" iterative method. The present study adopts the SIMPLE (Patankar and Spalding, 1972) algorithm to calculate the pressure field.

The iterative solution may be generally considered to have converged when the sum of the normalised absolute residuals across all nodes is less than a prescribed small value δ,

$$\frac{\sum \left| \sum_{nb} A_{nb}\phi_{nb} + S_U - A_P\phi_P \right|}{\phi_{inlet}} \leq \delta \quad (18)$$

In our computations, we set δ to be 10^{-4}.

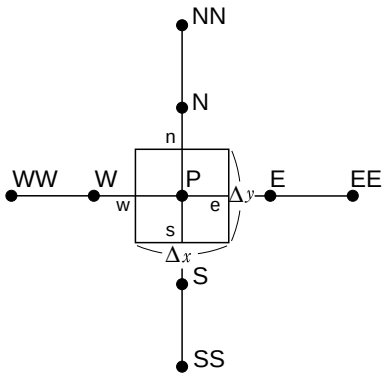

Figure 1.
Two-dimensional control volume

3.2 Grids generation

In order to produce a smooth distribution of grid lines, (ξ, η), in the flow domain, the Poisson equations representing these grid lines are solved iteratively.

$$\frac{\partial^2 \xi}{\partial x^2} + \frac{\partial^2 \xi}{\partial y^2} = -a_1 e^{-\alpha_1|\xi-\xi_1|} - a_2 e^{-\alpha_2|\xi-\xi_2|} \tag{19}$$

$$\frac{\partial^2 \eta}{\partial x^2} + \frac{\partial^2 \eta}{\partial y^2} = -b_1 e^{-\beta_1|\eta-\eta_1|} - b_2 e^{-\beta_2|\eta-\eta_2|} \tag{20}$$

Here $\xi = \xi(x, y)$ and $\eta = \eta(x, y)$, where ξ is in the general streamwise direction and η is in the direction as nearly orthogonal to ξ as possible. After initial distribution of the grid lines, further refinement is carried out around the sharp corners of the wall; along each (constant) ξ line originating from the wall, the η lines are redistributed according to $\eta_j = \eta_1 q^{j-1}$ where starting from the wall, q is a prescribed ratio of the consecutive η grid line spacing. In doing so, there are much more resultant grid lines close to the upper and lower walls for better resolution of the flow features.

4. Results and discussion

The numerical solutions are carried out for an axisymmetric diffuser with a back-facing curved surface centre-body, where experimental data are available from references Xu (1995a; 1995b). In the experiments, the hot wire was used to measure the velocity and turbulent intensity distribution at various locations in the axisymmetric diffuser. In order to determine the separation and reattachment points on the centre-body, an oil film flow visualisation technique was employed. The results obtained were confirmed independently following the use of tuft to locate the separation and reattachment points to well within $\pm 10\% H$. (Here H is the height of the back-facing curved step, 16.875mm in height, which is also used to normalise all the lengths in the calculations (see Figure 2). This, in turn, is in general agreement with the overall measured velocity distributions. It should be pointed out that the experimental flow Reynolds number, based on H and incoming free stream velocity, is 2.0×10^4.

In this work, our focus is mainly on the experimentally obtained separation and reattachment locations for direct comparison to the different turbulence

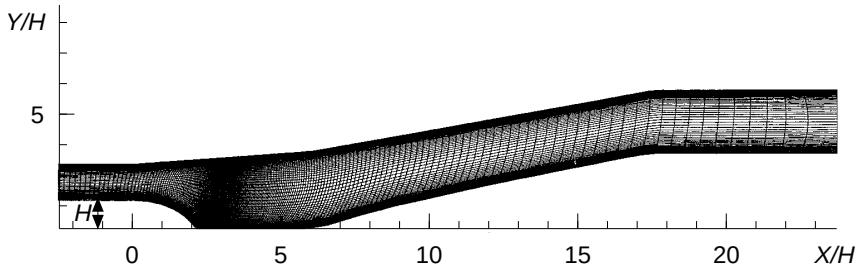

Figure 2.
Geometry and mesh

models used in the numerical simulations. The interested reader should refer to Xu (1995a; 1995b) for experimental details.

4.1 Grid independence

The grid independence of the numerical results is examined before the main calculations are carried out. The test case selected using the high-Reynolds k-ε turbulence model with wall function model is repeatedly calculated with seven kinds of grids from coarse to fine. The separation and reattachment locations of streamlines denoted by X_S/H and X_R/H respectively, are computed and compared for different grid sizes. From Table I, a convergence to grid independence is fairly obvious. It is reckoned that the result from a 200×70 grid is sufficiently accurate for prediction purposes because the separation and reattachment locations for the 200×70 grid differ from the 300×70 grid by less than 2.4 and 1.3 per cent respectively. The former uses much less CPU time than the latter by about a factor of 0.45.

From the above, further computations pertaining to different turbulence models are carried out for the typical grid size of 200×70, which is shown in Figure 2. It may be noted that more grid lines are distributed near to the solid wall and back-facing curved surface region to reflect the expected rapid changes or much sharper velocity gradients of the flow field.

4.2 Results of high-Reynolds k-ε *+ wall function model*

In the first calculation, the high-Reynolds number k-ε turbulence model is used to deal with the turbulent flow in the main flow region, and the wall function method to treat the flow near the wall where the assumption for the application of the high-Reynolds number turbulence model is no longer valid.

The geometry of the grids is shown in Figure 2. The upper and lower edges correspond to the solid wall; the left is the flow entry and the right is the exit region. The inlet conditions are taken from velocity measurements (Xu 1995a; 1995b). The under-relaxation iteration technique is adopted to increase numerical stability with relaxation factors $\alpha_u = \alpha_v = \alpha_k = \alpha_\varepsilon = 0.5$ and $\alpha_p = 0.7$.

The final convergent result is obtained after 3,270 iterations. Figure 3 shows the locally enlarged streamline distributions around the backward curved surface. It can be clearly observed that there is a recirculation zone developed

Table I.
Grid independent test

Mesh	X_S/H	X_R/H	Relative CPU time
80×40	1.459	6.619	0.192
100×50	1.411	6.215	0.325
150×60	1.363	6.616	0.577
175×70	1.332	6.658	0.824
200×70	1.332	6.598	1.000
250×70	1.293	6.583	1.614
300×70	1.301	6.512	2.200

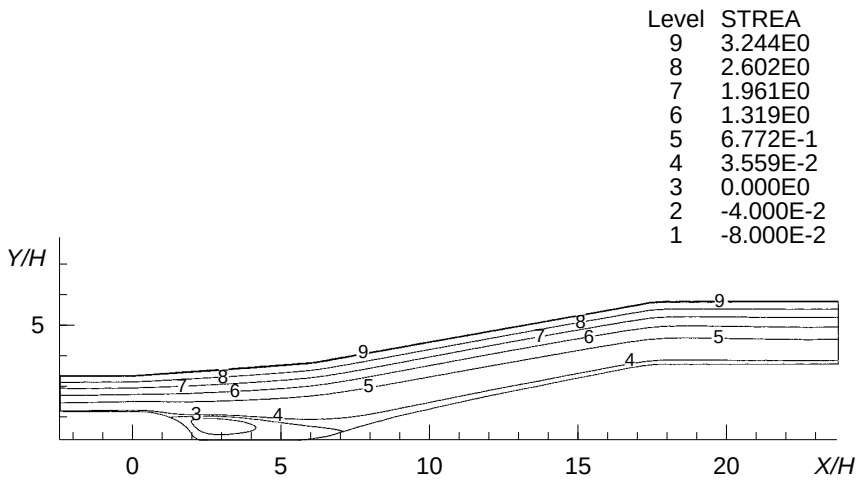

Figure 3.
Streamlines, high-Reynolds k-ε + wall function model

just behind the curved surface. The separation starts at the curved surface and reattachment occurs downstream. (This is sometimes referred to as separation bubble.) The separation and reattachment positions are listed in Table II together with the experiments and other turbulence models (see below) for the purpose of comparison.

For the purpose of completeness, Figures 4 and 5 give the local enlarged velocity vectors and pressure contours around back-facing curved surface inside the diffuser.

4.3 Results of high-Reynolds k-ε *+ one-equation model*

This is sometimes called the zonal modelling. The computational domain is divided into two regions. The high-Reynolds number k-ε model is used in the main flow region, and one-equation turbulence model (Wolfshtein's model) is adopted in the region near the wall.

The same distribution of ξ and η lines as in Section 4.1 is used for this model. On the upper wall, the wall function method is still being used instead of

Model	X_S/H	X_R/H	Relative CPU time
Test	1.78	7.50-8.00	–
High Re k-ε + wall function	1.332	6.598	1.0
High Re k-ε + one equation	1.638	7.991	4.0 (10.0)[a]
Low Re k-ε	1.332	7.170	12.0 (28.0)[a]
RNG k-ε	1.031	10.308	1.4
Anisotropic k-ε (Launder)	1.415	6.865	19.0

Note:
[a] The relative CPU time in brackets refers to the full employment of respective models on both the upper and lower walls

Table II.
Separation and reattachment positions

Wolfshtein's model, since the main interest is in the flow region around and near the central body. (This approach is taken primarily to reduce CPU time required. If Wolfshtein's model is applied to both the upper and lower walls, the CPU time required is about doubled but with almost the same level of numerical accuracy for the prediction of the separation and reattachment positions on the lower wall. A closer examination of the resultant flow field reveals that there is no separation on the upper wall, and may further suggest that the flow near the upper wall in the present geometry has little or no influence on the flow separation or reattachment on the lower wall.) The boundary conditions and the under-relaxation factors used are the same as before.

The final convergent result is obtained after 16,485 iterations. The general patterns of streamline, velocity vectors and pressure contours around the back-facing curved surface are about the same as the ones obtained by high-Reynolds number k-ε model. Therefore, they are not shown here. The possibly notable differences are the separation and reattachment positions which are also listed in Table II for comparison.

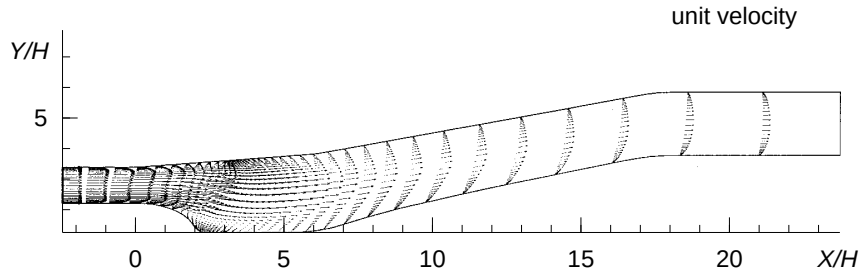

Figure 4.
Velocity, high-Reynolds k-ε + wall function model

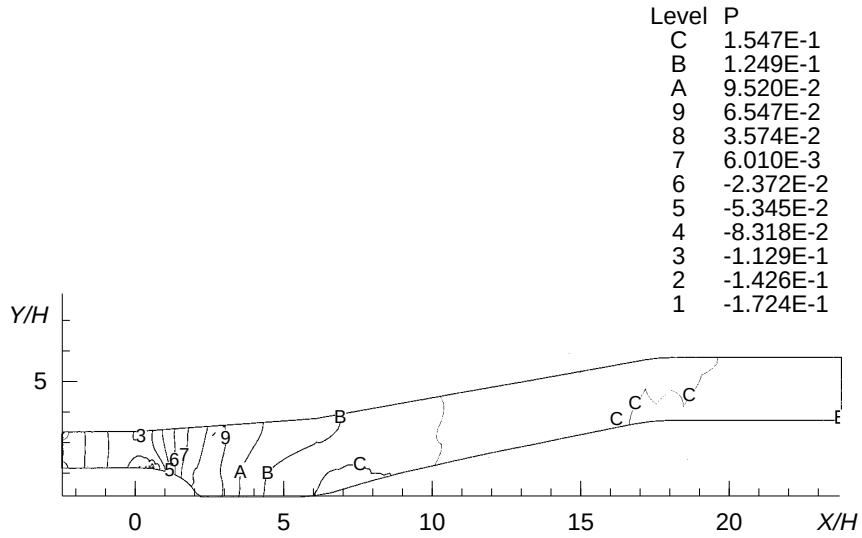

Figure 5.
Pressure, high-Reynolds k-ε + wall function model

4.4 Results of low-Reynolds k-ε *model*

In this section, the low-Reynolds number Launder-Sharma turbulence model is used to calculate the turbulent flow. In order to reduce CPU time, the high Reynolds number k-ε and wall function model is used to deal with the flow near the upper wall region as our main interest is the flow around the centre-body. This is similar to the approach taken in Section 4.3. However, if the low-Reynolds number Launder-Sharma turbulence model is applied to both the upper and lower walls, the separation and reattachment positions on the lower centre body differ by less than 1.0 per cent which supports the notion of minimal influence of the upper wall on the flow in the lower wall for the present geometry. The CPU time taken, on the other hand, has increased by more than 100 per cent)

The under-relaxation factors for u, v, p, k and ε are 0.2, 0.2, 0.1, 0.2 and 0.2 respectively. The final convergent result is obtained after more than 46,000 iterations. Again, since there is no salient difference in the general distribution of the streamlines, velocity vectors and pressure contours between this turbulence model and the high Reynolds number k-ε and wall function calculation, the results of the former are not shown here except for the separation and reattachment positions which are indicated in Table II for detailed comparison.

4.5 Results of RNG k-ε *model*

The RNG k-ε turbulence model is applied to calculate the turbulent flow in this section. The mesh used in this model is exactly the same as the one used in the low Reynolds number k-ε turbulence model.

The numerical stability of this model is quite good. Therefore, the under-relaxation factors for u, v, p, k and ε are chosen as 0.5, 0.5, 0.7, 0.5 and 0.5 respectively. The final convergent result is obtained after more than 4,512 iterations. The general distributions of the streamline patterns, velocity vectors and pressure contours do not differ significantly from the corresponding plots in Figures 3, 4 and 5 respectively, except for a visibly bigger size separation bubble; the former results are not presented here. On the other hand, to account for the observed difference in the separation bubble size, the separation and reattachment positions are listed in Table II. From Table II, it is clear that this model predicts a very early separation and a delayed reattachment when compared to the experiments and the other turbulence models.

4.6 Results of anisotropic k-ε *model*

Finally, the anisotropic k-ε turbulence model with Launder and Suga's eddy-viscosity equation (Launder and Suga, 1993) is used to calculate the turbulent flow. With the presence of the curved surface, the flow in the diffuser is supposedly a case of strong anisotropic turbulent flow. For the better prediction of such flow, one may want to consider the anisotropic feature of the flow.

The under-relaxation factors for u, v, p, k and ε are 0.1, 0.1, 0.1, 0.1 and 0.1, respectively. The separation and reattachment positions are listed in Table II. It

can be seen from the table that the model does not give a significantly better prediction compared to the experiments although one may expect otherwise since flow anisotropy has been accounted for in this turbulence model. However, judging from the general distributions of the streamline patterns, velocity vectors and pressure contours which only indicate fairly minor differences from the corresponding plots computed using the other turbulence models (for example, see Figures 3-5) and thus the said results are not presented here, it may be suggested that the flow geometry selected in this test case may not possess sufficiently strong "anisotropy" to warrant the use of the anisotropic k-ε turbulence model with its associated high computational cost.

From Table II, there are apparently significant differences among the various turbulent models in predicting the locations of the separation and reattachment points. Perhaps this is not too surprising in view of the fact that an accurate prediction hinges primarily on the model's ability to resolve the interaction between the surface wall curvature and the state of turbulence. In the present study, we have merely adopted the commonly employed general turbulence models available in the literature. It may be noted too that Lien and Leschziner (1994a; 1994b) employed several turbulence models (some of which are identical to this work) to compute the reattachment position of a 2D turbulent flow over a much simpler flat surface backward facing step for a similar range of Reynolds number (based on free stream velocity and step height) for comparison to experiments. Of course, in their investigations, flow separation occurs right at the back-facing step. Despite this employment of the general turbulence models, results from Figures 3-5 and Table II still clearly suggest that the high Reynolds number k-ε + Wolfshtein's one-equation turbulence model presents the best prediction for separation and reattachment positions for the present flow configuration. All the calculations, however, predict an earlier separation position than the experiment although the said result obtained with the high-Reynolds number k-ε + Wolfshtein's one-equation turbulence model is well within the experimental uncertainty of about 10 per cent.

5. Conclusion

Turbulent flows inside an axisymmetric diffuser are numerically studied in the present study by using five different turbulent models: high-Reynolds number k-ε + wall function model; high-Reynolds number k-ε + one-equation model; low-Reynolds number k-ε model; RNG turbulence model; and anisotropic turbulence model. From the numerical calculations and comparisons between numerical solutions and experimental measurements, the following conclusions can be drawn.

- High-Reynolds number k-ε + wall function model uses the least CPU time.
- High-Reynolds number k-ε + one-equation model gives the best numerical prediction for the separation and reattachment positions. It also requires reasonable CPU time.

- High-Reynolds number k-ε + wall function model, low-Reynolds number k-ε Launder-Sharma's model and anisotropic model greatly under-predict the separation position by at least 25 per cent.
- Low-Reynolds number k-ε Launder-Sharma's model uses rather substantial CPU time but does not lead to significant improvement in the numerical predictions.
- RNG turbulence model predicts a bigger separation bubble in the present numerical study. It gives a very early separation point and delayed reattachment point.
- Among the five models, the anisotropic turbulence model uses the longest CPU time. However, this model does not present the best prediction for the separation and reattachment positions.
- All the models predict an earlier separation than the experiment.

References

Launder, B.E. and Sharma, B.I. (1974), "Applicating the energy-dissipation model of turbulence to flow over a spinning disc", *Letters in Heat and Mass Transfer*, Vol. 1, p. 131.

Launder, B.E. and Spalding, D.B. (1972), *Mathematical Models of Turbulence*, Academic, New York, NY.

Launder, B.E. and Spalding, D.B. (1974), "The numerical computation of turbulent flow", *Comp. Mech. in Appl. Mech. and Eng.*, Vol. 3, p. 269.

Launder, B. E. and Suga, K. (1993), "Extending the applicability of eddy viscosity models through the use of deformation invariant and non-linear elements", *Proceedings of the Fifth IAHR Conference on Refined-Flow and Turbulence Measurement*, Paris.

Launder, B.E., Morse, A., Rodi, W. and Spalding, D.B. (1972), "The prediction of free shear stress flows – a comparison of the performance of six turbulent models", *Proc. Langley Free Shear Flows Conf.*, NASA SP320.

Lien, F.S. and Leschziner, M.A. (1994a), "A general non-orthogonal collocated finite volume algorithm for turbulent flow at all speeds incorporating second-moment turbulence-transport closure, part 2: application", *Comput. Methods Appl. Mech. Engrg.*, Vol. 114, pp. 149-67.

Lien, F.S. and Leschziner, M.A. (1994b), "Sensitivity of 2D separation characteristics to turbulence modelling, *Sixth Biennial Colloquium on Computational Fluid Dynamics*, Mech. Eng. Dept., UMIST, 25-26 May.

Patankar, S.V. and Spalding, D.B. (1972), "A calculation procedure for heat, mass, and momentum transfer in three-dimensional flows", *Int. J. Heat Mass Transfer*, Vol. 15, p. 1787.

Wolfshtein, M. (1969), "The velocity and temperature distribution in one-D flow with turbulence augmentation and pressure gradient", *Int. J. Heat Mass Transfer*, Vol. 12, pp. 139-63.

Xu, D. (1995a), "Turbulent flow pass curved surfaces, part 1: experimental study", Tech. Report, Mech. Eng. Dept., UMIST.

Xu, D. (1995b)., "Turbulent flow pass curved surfaces, part 2: computational study", Tech. Report, Mech. Eng. Dept., UMIST.

Yakhot, V., Orszag, S.A., Thangam, S., Gatski, T.B. and Speziale, C.G. (1992), "Development of turbulence models for shear flows by a double expansion technique", *Physics of Fluids*, Vol. A4 No. 7, pp. 1510-20.